

# Atomic vacancies of molybdenum disulfide nanoparticles stimulate mitochondrial biogenesis

Received: 13 August 2023

Accepted: 2 September 2024

Published online: 17 September 2024


 Check for updates

Kanwar Abhay Singh <sup>1</sup>, John Soukar <sup>1,2</sup>, Mohammad Zulkifli <sup>3</sup>, Anna Kersey<sup>1,4</sup>, Giriraj Lokhande<sup>1</sup>, Sagnika Ghosh <sup>3</sup>, Aparna Murali<sup>1,4</sup>, Natalie M. Garza<sup>3</sup>, Harman Kaur<sup>3</sup>, Justin N. Keeney <sup>5</sup>, Ramu Banavath <sup>1,4</sup>, Hatice Ceylan Koydemir <sup>1,4</sup>, Raquel Sitcheran <sup>2,5</sup>, Irtisha Singh <sup>1,2,5</sup> , Vishal M. Gohil <sup>2,3</sup>  & Akhilesh K. Gaharwar <sup>1,2,5,6</sup> 

Diminished mitochondrial function underlies many rare inborn errors of energy metabolism and contributes to more common age-associated metabolic and neurodegenerative disorders. Thus, boosting mitochondrial biogenesis has been proposed as a potential therapeutic approach for these diseases; however, currently we have a limited arsenal of compounds that can stimulate mitochondrial function. In this study, we designed molybdenum disulfide (MoS<sub>2</sub>) nanoflowers with predefined atomic vacancies that are fabricated by self-assembly of individual two-dimensional MoS<sub>2</sub> nanosheets. Treatment of mammalian cells with MoS<sub>2</sub> nanoflowers increased mitochondrial biogenesis by induction of PGC-1 $\alpha$  and TFAM, which resulted in increased mitochondrial DNA copy number, enhanced expression of nuclear and mitochondrial-DNA encoded genes, and increased levels of mitochondrial respiratory chain proteins. Consistent with increased mitochondrial biogenesis, treatment with MoS<sub>2</sub> nanoflowers enhanced mitochondrial respiratory capacity and adenosine triphosphate production in multiple mammalian cell types. Taken together, this study reveals that predefined atomic vacancies in MoS<sub>2</sub> nanoflowers stimulate mitochondrial function by upregulating the expression of genes required for mitochondrial biogenesis.

Mitochondria generate cellular energy in the form of adenosine triphosphate (ATP) via oxidative phosphorylation (OXPHOS), which is carried out by the mitochondrial respiratory chain (MRC) and ATP synthase. Mitochondrion is the only organelle with an independent genome, and its replication and function rely on the transcription of genes within both the nuclear and mitochondrial genomes. Given its central role in cellular metabolism, defects in mitochondrial

bioenergetics are associated with a number of rare inheritable disorders of energy metabolism<sup>1,2</sup> as well as common age-related diseases including cancer, type 2 diabetes<sup>3,4</sup>, osteoporosis<sup>5</sup> and neurodegenerative disorders such as Parkinson's and Alzheimer's<sup>6,7</sup>. Although several mitochondria-targeting therapeutics have been developed, they suffer from limited efficacy, high toxicity, and inadequate bioavailability<sup>8,9</sup>.

<sup>1</sup>Department of Biomedical Engineering, College of Engineering, Texas A&M University, College Station, TX, USA. <sup>2</sup>Interdisciplinary program in Genetics and Genomics, Texas A&M University, College Station, TX, USA. <sup>3</sup>Department of Biochemistry and Biophysics, College of Agriculture & Life Sciences, Texas A&M University, College Station, TX, USA. <sup>4</sup>Center for Remote Health Technologies and Systems, Texas A&M Engineering Experiment Station, College Station, TX, USA. <sup>5</sup>Department of Cell biology and Genetics, College of Medicine, Texas A&M University, Bryan, TX, USA. <sup>6</sup>Department of Material Science and Engineering, College of Engineering, Texas A&M University, College Station, TX, USA.  e-mail: [isingh@tamu.edu](mailto:isingh@tamu.edu); [vgohil@tamu.edu](mailto:vgohil@tamu.edu); [gaharwar@tamu.edu](mailto:gaharwar@tamu.edu)

To address this challenge, we propose utilizing atomic scale modification of two-dimensional (2D) nanomaterials to boost mitochondrial biogenesis. Ultrathin 2D nanomaterials have an extremely high surface-to-volume ratio compared to other nanomaterials and exhibit high surface energy<sup>10</sup>. This increase in surface energy of 2D nanomaterials has been shown to enhance their catalytic activity, which can be leveraged in biological systems to modulate cellular metabolism<sup>11</sup>. In many cases, the basal plane of the nanomaterial remains chemically inert, while the edges act as active sites for catalytic activity<sup>12</sup>. By incorporating empty sites within the atomic lattice of 2D nanomaterials (i.e., atomic vacancies), it is possible to create structural defects that can result in an increase of active sites for catalysis<sup>13</sup>. Here, we selected transition metal dichalcogenide (TMD), which are an emerging class of ultrathin 2D nanomaterials with a high degree of anisotropy and chemical functionality<sup>14,15</sup>. Transition metals play a crucial role in cellular homeostasis and serve as cofactors in enzymatic reactions, as they can readily transition between oxidized and reduced states<sup>16,17</sup>. Transition metals such as molybdenum (Mo) are essential for nearly all organisms and form the catalytic centers of several metalloenzymes<sup>18</sup>. Mo shuttles between three versatile oxidation states (+4, +5, and +6) and is crucial for catalyzing redox reactions<sup>18</sup>. These characteristics provide a strong basis for synthesizing TMD nanoparticles for the purpose of modulating mitochondrial function. Molybdenum disulfide (MoS<sub>2</sub>) is a promising TMD nanomaterial and has attracted significant interest in biomedicine due to its superior electrochemical<sup>12,19–21</sup> and photo-responsive characteristics<sup>22</sup>. MoS<sub>2</sub> comprises of one layer of molybdenum (Mo) oriented between two sulfur (S) layers with a strong covalent bond. MoS<sub>2</sub> can boost electrocatalytic performance by enhancing electrochemical kinetics and low-loss electrical transport<sup>12,19–21</sup>.

Given the high cyto- and biocompatibility of MoS<sub>2</sub><sup>23</sup>, along with its unique structure and efficient electrochemical characteristics, we propose designing atomic vacancy-rich 2D MoS<sub>2</sub> nanomaterials to explore their role in modulating mitochondrial function. Here, we show MoS<sub>2</sub> nanoflower with high atomic vacancies catalyze cellular reactive oxygen species (ROS). This reduction in cellular ROS levels results in the activation of the SIRT1/PGC-1 $\alpha$  pathway, leading to enhanced mitochondrial biogenesis and increased cellular respiration.

### Synthesis and characterization of MoS<sub>2</sub> nanoflowers with predefined atomic vacancies

To synthesize MoS<sub>2</sub> nanoflowers, molecular precursors of molybdenum (Hexaammonium heptamolybdate tetrahydrate) and sulfur (Thiourea) are used in a stoichiometric ratio of 1:2. After hydrothermal synthesis and removal of unreacted precursors and impurities, we obtain MoS<sub>2</sub> nanoflowers, which are composed of MoS<sub>2</sub> nanosheets. The individual MoS<sub>2</sub> nanosheets consist of a hexagonal lattice structure, where each layer is made of a covalently linked S–Mo–S nanosheet. These nanosheets are held together by short-range *van der Waals* interactions, resulting in their flower-like morphology<sup>23,24</sup>. Due to the planar MoS<sub>2</sub> lattice, it is possible to introduce additional atomic vacancies by altering the precursor ratio (Mo:S). We used a Mo:S ratio of 1:1 to incorporate a relatively low degree of atomic vacancies and 1:6 to incorporate a relatively high degree of atomic vacancies (or vacancy rich)<sup>23–25</sup> compared to a typical synthesis with a precursor ratio of 1:2. The morphology of the MoS<sub>2</sub> nanoflowers was characterized by transmission electron microscopy (TEM). The individual nanosheets were stacked together due to Ostwald ripening to form concentric, hierarchical flower-like structures ~200 nm in diameter (Fig. 1A). Thus, the introduction of atomic vacancy did not affect the morphology of the MoS<sub>2</sub> nanoflowers.

The crystallographic arrangement of the Mo and S atoms within the nanoflowers and the effect of atomic vacancies on the crystalline structure was determined by X-ray diffraction (XRD) spectroscopy. The diffraction peaks (002, 100, 110) of the MoS<sub>2</sub> nanoflowers indicate the presence of a hexagonal crystal structure, similar to hexagonal

MoS<sub>2</sub> (JCPDS card No. 73–1508) (Fig. 1A). The crystallite size of the nanoflowers was calculated using the Scherrer equation (using the 002 peak), and we observed nanoflowers with typical degree of atomic vacancies (1:2) and relatively low degree of atomic vacancies (1:1) had a crystallite size of 6.13 nm, while nanoflowers with relatively high degree of atomic vacancies (1:6) had a larger crystallite size of 7.59 nm. X-ray photoelectron spectra (XPS) analysis of the binding energies (BE) for Mo and S core-level electrons indicated the presence of Mo<sup>4+</sup> ( $3d^{5/2}$  - 228 eV and  $3d^{3/2}$  - 231 eV) and S<sup>2-</sup> ( $2p^{3/2}$  - 161 eV and  $2p^{1/2}$  - 162 eV) within MoS<sub>2</sub> nanoflowers with predefined atomic vacancies (Fig. 1B). Further deconvolution of the XPS spectra indicated the presence of predominantly 2H phase (hexagonal symmetry) within the trigonal prismatic MoS<sub>2</sub> crystal (1T phase). This suggests that the incorporation of atomic vacancies did not cause appreciable changes in the morphology or crystal structure of the MoS<sub>2</sub> nanoflowers. The increased density of active centers (sites of atomic vacancy) within the nanoflowers was verified using cyclic voltammetry. The density of active sites in the high atomic vacancy nanoflowers (1:6) was determined to be  $5.59 \times 10^{-4}$  moles g<sup>-1</sup>, with the overall trend being similar to that reported in our earlier studies<sup>24</sup> (Fig. 1C). The increase in active sites also results in enhanced catalytic decomposition of hydrogen peroxide (H<sub>2</sub>O<sub>2</sub>) by the nanoflowers. This was evaluated using electrochemical (amperometric evaluation of H<sub>2</sub>O<sub>2</sub> reduction) and biochemical (catalase enzyme activity) assays respectively, with both assays indicating nanoflowers with high atomic vacancies (MoS<sub>2</sub> (1:6)) exhibiting enhanced catalytic activity as compared to the other formulations (Supplementary Fig. 1).

To determine the effect of atomic vacancies on aqueous stability, the zeta potential of MoS<sub>2</sub> nanoflowers was evaluated in deionized water (DI) and cell culture media containing fetal bovine serum (FBS) (Figure S2). In DI water, MoS<sub>2</sub> nanoflowers exhibited a strong negative zeta potential of  $-33.58 \pm 0.39$  mV. The introduction of atomic vacancies resulted in a slight increase in zeta potential to  $-29.32 \pm 0.511$  mV for (1:1) and  $-30.5 \pm 2$  mV for (1:6) MoS<sub>2</sub> nanoflowers, respectively. However, in cell culture media the zeta-potential of all three types of nanoflowers showed an increase ( $-11.5 \pm 0.5$  mV). This change is attributed to the adsorption of proteins onto the surface of the nanoflowers and resultant charge shielding. The adsorbed proteins on the MoS<sub>2</sub> nanoflowers were evaluated by Sodium Dodecyl Sulfate–Polyacrylamide Gel Electrophoresis (SDS-PAGE). Analysis of the protein bands indicated that the degree of atomic vacancies within the nanoflowers does not impact the type of proteins absorbed (Supplementary Fig. 2).

Cellular compatibility of the MoS<sub>2</sub> nanoflowers was determined by measuring cellular DNA content in human mesenchymal stem cells (hMSCs) cells post 24 h of exposure to the nanoflowers (Fig. 1D). The concentration of MoS<sub>2</sub> nanoflowers, at which the cell viability is reduced by 50%, was regarded as the half-maximal inhibitory concentration (IC<sub>50</sub>) as determined by fitting a logarithmic dose-response curve. All variations of MoS<sub>2</sub> were highly cytocompatible, as evident from a high IC<sub>50</sub> value (~400  $\mu$ g/mL), with no significant effect of degree of atomic vacancies on cytocompatibility observed. The cellular compatibility of MoS<sub>2</sub> nanoflowers was similar to other biocompatible nanoparticles such as graphene, hydroxyapatite, bioglass, and gold nanoparticles<sup>26</sup>. The integrity of the cell membrane was evaluated by measuring the release of the cytosolic enzyme lactate dehydrogenase (LDH) in the cell culture media. No significant release of LDH was observed from cells treated with concentrations up to 200  $\mu$ g/mL of MoS<sub>2</sub>, indicating the presence of an intact plasma membrane (Fig. 1E). The effect of MoS<sub>2</sub> nanoflowers on various cell cycle stages was evaluated by treating hMSCs with 25–100  $\mu$ g/mL of MoS<sub>2</sub> nanoflowers for 72 h (Fig. 1F). While a MoS<sub>2</sub> concentration of 25  $\mu$ g/mL produced no significant cell cycle alteration, an observable reduction in the S and G2/M phase was noted at doses exceeding 50  $\mu$ g/mL, suggesting that higher concentrations of MoS<sub>2</sub> inhibit cell proliferation over time. Exposure of hMSCs to atomic

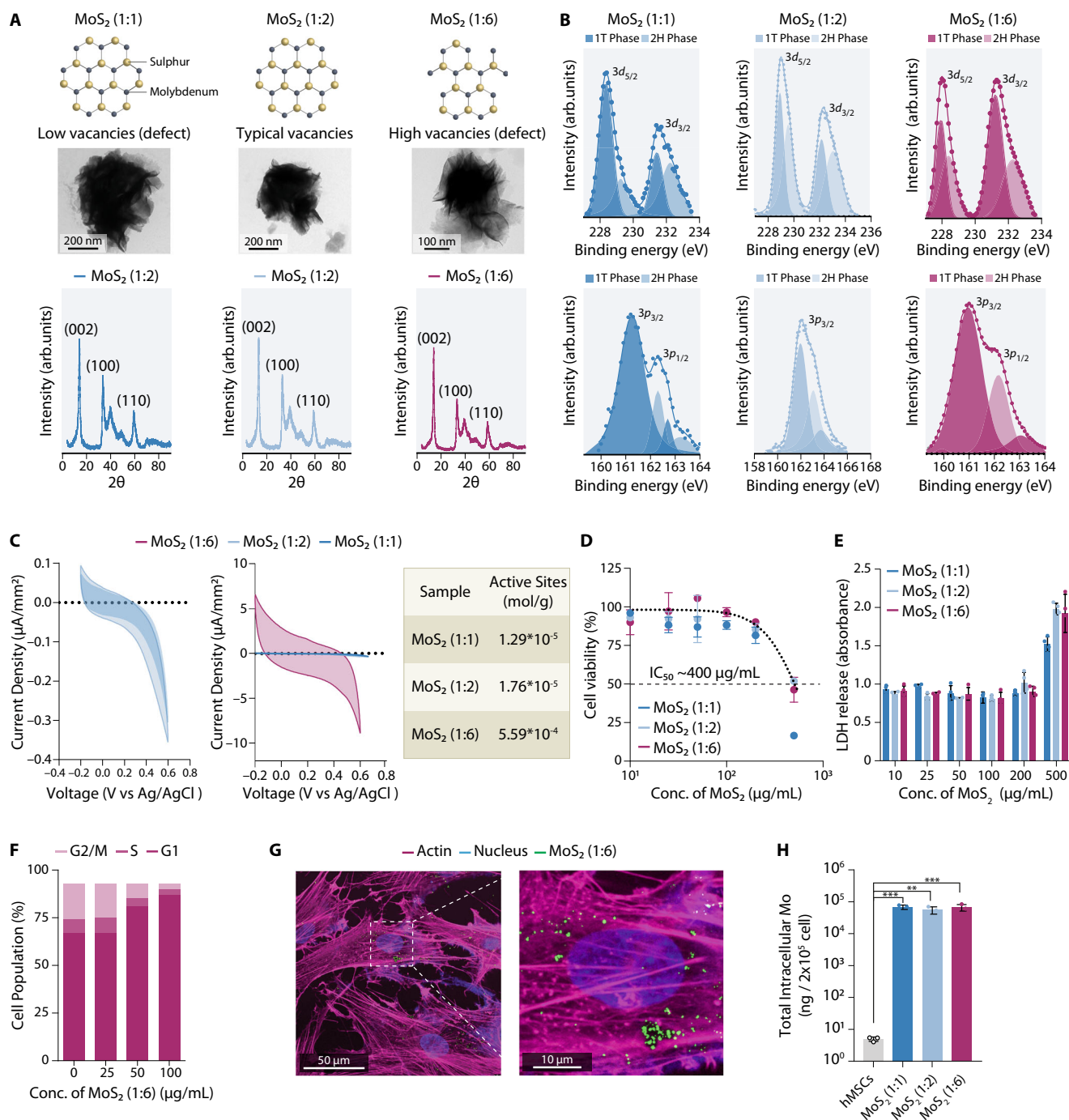


**Fig. 1 | Synthesis and characterization of MoS<sub>2</sub> nanoflowers with predefined atomic vacancies.** **A** Atomic arrangement of Mo and S in 2D MoS<sub>2</sub>. Changing molybdenum: sulfur precursor ratio leads to the formation of MoS<sub>2</sub> with different degrees of atomic vacancies. Transmission electron microscopy (TEM) images show MoS<sub>2</sub> nanoflower assembly consisting of multiple individual MoS<sub>2</sub> nanosheets. X-ray diffraction (XRD) peaks of MoS<sub>2</sub> nanoflowers (002, 100, 110) show the presence of hexagonal crystal structure. **B** X-ray photoelectron spectra (XPS) show the binding energies (BE) for Mo and S within MoS<sub>2</sub> nanoflowers. 1T (trigonal prismatic) and 2H phase (hexagonal symmetry) within the trigonal prismatic MoS<sub>2</sub> crystal. **C** Cyclic voltammograms for MoS<sub>2</sub> coated electrode in comparison with standard uncoated electrode. The density of active sites calculated from these voltammograms are presented in the table in moles/g. The density of active sites increases with increasing sulfur precursor ratio. **D** The effect of MoS<sub>2</sub> nanoflowers concentration (with differing degree of atomic vacancies) on cell viability in hMSCs following 24 h of exposure. MoS<sub>2</sub> nanoflowers exhibit half-inhibitory

concentration (IC<sub>50</sub>) of ~400 μg/mL. (data represented as mean ± SD, with *n* = 4 biological replicates). **E** Cell membrane integrity in presence of MoS<sub>2</sub> was determined by monitoring release of LDH in media following 24 h of exposure. No significant effect of atomic vacancies is observed at lower concentration (< IC<sub>50</sub>) of MoS<sub>2</sub> nanoflowers. (data represented as mean ± SD, with *n* = 4 biological replicates). **F** Effect of atomic vacancies of MoS<sub>2</sub> nanoflowers (1:6) on cell cycle is determined after 72 h. (data represented as average cell population within each phase of the cell cycle, with *n* = 3 biological replicates). **G** Internalization of MoS<sub>2</sub> nanoflower (1:6) is evident from fluorescence images of cells after 24 h. Green: MoS<sub>2</sub> nanoflowers, Purple: actin cytoskeleton. Blue: DAPI, nucleus. **H** Cellular internalization of MoS<sub>2</sub> nanoflowers was determined using ICP-MS elemental analysis following 18 h of exposure to nanoflowers. The levels of Mo are plotted for hMSCs treated with and without MoS<sub>2</sub> nanoflowers. (Data represented as mean ± SD, with *n* = 3 biological replicates. Statistical significance was determined using one way ANOVA with post hoc Tukey test, \**p* < 0.05; \*\**p* < 0.01, \*\*\**p* < 0.001).

vacancy rich nanoflowers at a concentration of 25  $\mu\text{g}/\text{mL}$  showed no significant changes in long term cell proliferation (Supplementary Fig. 3A). The internalization process of  $\text{MoS}_2$  nanoflowers by cells was assessed using F-actin and nuclear fluorescence staining, and the  $\text{MoS}_2$  nanoflowers were visualized via reflective light (Fig. 1G). Additionally, TEM was used to visualize the nanoflower uptake, with the TEM micrographs of internalized nanoflowers indicating the localization of nanoflowers within endosomal vesicles (Supplementary Fig. 4). The extent of cellular internalization of  $\text{MoS}_2$  nanoflowers was further quantified by inductively coupled plasma mass spectroscopy (ICP-MS) based elemental analysis. After 18 h of incubation with  $\text{MoS}_2$  nanoflowers (25  $\mu\text{g}/\text{mL}$ ), there was a pronounced increase in intracellular Mo, which was unaffected by the degree of atomic vacancy (Fig. 1H). Following these in vitro observations, all subsequent cellular studies with  $\text{MoS}_2$  nanoflowers were conducted at a concentration of 25  $\mu\text{g}/\text{mL}$  unless otherwise mentioned.

### Atomic vacancies alter the cellular transcriptomic profile

To investigate the effect of atomic vacancies on transcriptome, we performed whole transcriptome sequencing (RNA-seq) of hMSCs treated with  $\text{MoS}_2$  (1:1 and 1:6) at a concentration of 25  $\mu\text{g}/\text{mL}$  for 7 days. The cells treated with  $\text{MoS}_2$  nanoflowers showed substantial differences in their transcriptome profiles as evident from principal component analysis (PCA) of differentially expressed genes (DEGs) (Fig. 2A, Supplementary Dataset 1–3). PCA of the 20% most variable genes (assessed by median absolute deviation) from the study group revealed a pronounced distinction (represented by PC1, accounting for 59.90% of the total variance) between hMSCs treated with and without  $\text{MoS}_2$  having different atomic vacancies. PC2 further accounted for 26.02% of the variance, adding to the interpretability of the data. In addition, the PCA and linear correlation analysis showed limited variation within the control and treatment group replicates (Supplementary Fig. 5). We further identified DEGs between treated and untreated hMSCs as described in our previous study<sup>27</sup>. We found that the treatment of hMSCs with low atomic vacancies  $\text{MoS}_2$  (1:1) significantly ( $P\text{-adj} < 0.01$ ) affected the expression of 1047 genes (454 upregulated and 593 downregulated, Fig. 2B). While for cells treated with  $\text{MoS}_2$  with high atomic vacancies (1:6), the expression profile of 1959 genes changed significantly (916 upregulated and 1043 downregulated genes) respectively (Fig. 2B–C).

The key biological processes that were affected by  $\text{MoS}_2$  treatment were identified via Gene Ontology (GO) enrichment analysis. GO enrichment analysis hierarchically classifies gene and gene products, utilizing statistical tests (hypergeometric test) to identify modulated cellular processes across samples<sup>28,29</sup>. For cells exposed to high atomic vacancy  $\text{MoS}_2$  (1:6), we refined the significant GO terms ( $P < 0.05$ ) using semantic similarity as a criterion. This process, which prioritizes GO terms with shared meaning, facilitated the formation of seven comprehensive clusters: morphogenesis, extracellular matrix, cell-matrix regulation, cellular locomotion component, mitochondrial electron chain transport, triphosphate metabolism, and protein catabolic targeting membrane (Fig. 2D). Similarly, for cells treated with low atomic vacancy  $\text{MoS}_2$  (1:1) GO terms such as extracellular matrix, cell-matrix regulation, and cellular locomotion component were enriched (Supplementary Fig. 6). Notably, two of the broader GO term clusters relating to biological processes primarily involved in cellular metabolism and respiration, were observed only in cells treated with  $\text{MoS}_2$  having high atomic vacancies (1:6). Some of these uniquely regulated GO terms pointed to genes encoding OXPHOS proteins, including mitochondrial respiratory chain complex assembly (GO:0033108), mitochondrial respiratory chain complex I assembly (GO:0032981), mitochondrial electron transport (GO:0006120), and ATP synthesis coupled electron transport (GO:0042773) (Supplementary Fig. 7).

### High atomic vacancies of $\text{MoS}_2$ upregulate transcription of nuclear-encoded mitochondrial genes

In order to understand the effect of atomic vacancies of  $\text{MoS}_2$  on nuclear-encoded mitochondrial genes, a selective inspection of the DEGs was performed using the MitoCarta 3.0 dataset, which is a curated repository of 1136 mitochondrial proteins<sup>30</sup>. hMSCs treated with high atomic vacancy  $\text{MoS}_2$  showed consistent upregulation of mitochondrial genes as compared to untreated cells (Fig. 3A). Treatment with high atomic vacancy  $\text{MoS}_2$  also resulted in the stimulation of biological processes such as Mitochondrial ATP synthesis coupled proton transport (GO:004277) and Mitochondrial electron transport (GO:0006123) (Fig. 3B). Within these processes, we observed a significant upregulation of OXPHOS genes such as *ATP5E* (fold change =  $2^{1.31}$ ,  $P\text{-adj} < 0.01$ ) and *COX5A* (fold change =  $2^{1.39}$ ,  $P\text{-adj} < 0.01$ ) (Fig. 3C). Analysis of DEGs in cells treated with high atomic vacancy  $\text{MoS}_2$  indicated a global upregulation of genes involved in OXPHOS complexes I, IV, V and mitochondrial protein synthesis, respectively (Supplementary Fig. 8). This data indicates that treatment with high atomic vacancy  $\text{MoS}_2$  results in an enhanced expression of genes involved in mitochondrial biogenesis.

To ensure the robustness of our RNA-Seq analysis, we employed Gene Set Enrichment Analysis (GSEA)<sup>31</sup>. GSEA of cells exposed to  $\text{MoS}_2$  with high atomic vacancies indicated a significant upregulation (normalized enrichment score (NES)  $> 1$ ) of processes relating to OXPHOS, which correlated well with our GO enrichment analysis (Fig. 3D). Particularly, the *Hallmark* gene sets *Oxidative Phosphorylation* (NES = 2.67,  $P\text{-adj} < 0.05$ ), *Fatty Acid Metabolism* (NES = 1.4,  $P\text{-adj} < 0.1$ ), and *Reactive Oxygen Species Pathways* (NES = 1.6,  $P\text{-adj} < 0.05$ ) showed a positive correlation (Fig. 3E), indicating mitochondrial energy metabolism and cellular reactive oxygen species (ROS) homeostasis as key cellular processes affected by the treatment with high atomic vacancy  $\text{MoS}_2$ . The subcellular localization of  $\text{MoS}_2$  nanoflowers was evaluated using confocal microscopy and revealed no colocalization between the nanoflowers and mitochondria (Fig. 3F), suggesting their influence extends to cytoplasmic targets to boost mitochondrial function and reduce cellular ROS. Additionally, these confocal images were used to perform mitochondrial morphology analysis using the Mito hacker pipeline<sup>32</sup> to determine the effect of  $\text{MoS}_2$  nanoflowers on mitochondrial morphology. The data thus generated indicated no significant change in mitochondrial network parameters such as mitochondrial branch length, mitochondrial area, and mitochondrial form factor following  $\text{MoS}_2$  nanoflower treatment (Fig. 3G).

### High atomic vacancies of $\text{MoS}_2$ stimulate mitochondrial biogenesis

The human mitochondrial genome is 16.6 kbp of circular double-stranded DNA, which encodes for 13 polypeptides that form essential components of the OXPHOS machinery as well as RNA molecules required for the translation of the mitochondrial DNA (mt-DNA) (Fig. 4A). Thus, to evaluate the effect of  $\text{MoS}_2$  with high atomic vacancies on mitochondrial function, we reverted to our RNA-seq dataset which showed an enhanced expression of all 13 mt-DNA encoded genes (Fig. 4B). Next, we assessed mt-DNA copy number in hMSCs by qRT-PCR analysis, which revealed a two-fold increase in relative mt-DNA levels in cells treated with high atomic vacancy  $\text{MoS}_2$  ( $\text{MoS}_2$  (1:6)) (Fig. 4C). Additionally, we observed a similar increase in mRNA expression of mt-DNA-encoded genes (such as *mt-ND2*) (Fig. 4C). To ensure the effect of  $\text{MoS}_2$  (1:6) treatment is not cell type specific, we evaluated the relative abundance of mt-DNA in MCF-7 and H9c2 cells treated with  $\text{MoS}_2$  (1:6) nanoflowers. We observed a similar trend in both cell lines, with cells treated with  $\text{MoS}_2$  (1:6) nanoflowers, exhibiting a nearly 2-fold increase of mt-DNA content compared to untreated cells (Supplementary Fig. 9). To investigate whether an increased expression of mt-DNA encoded genes translates into increased abundance of their respective proteins, we conducted SDS-



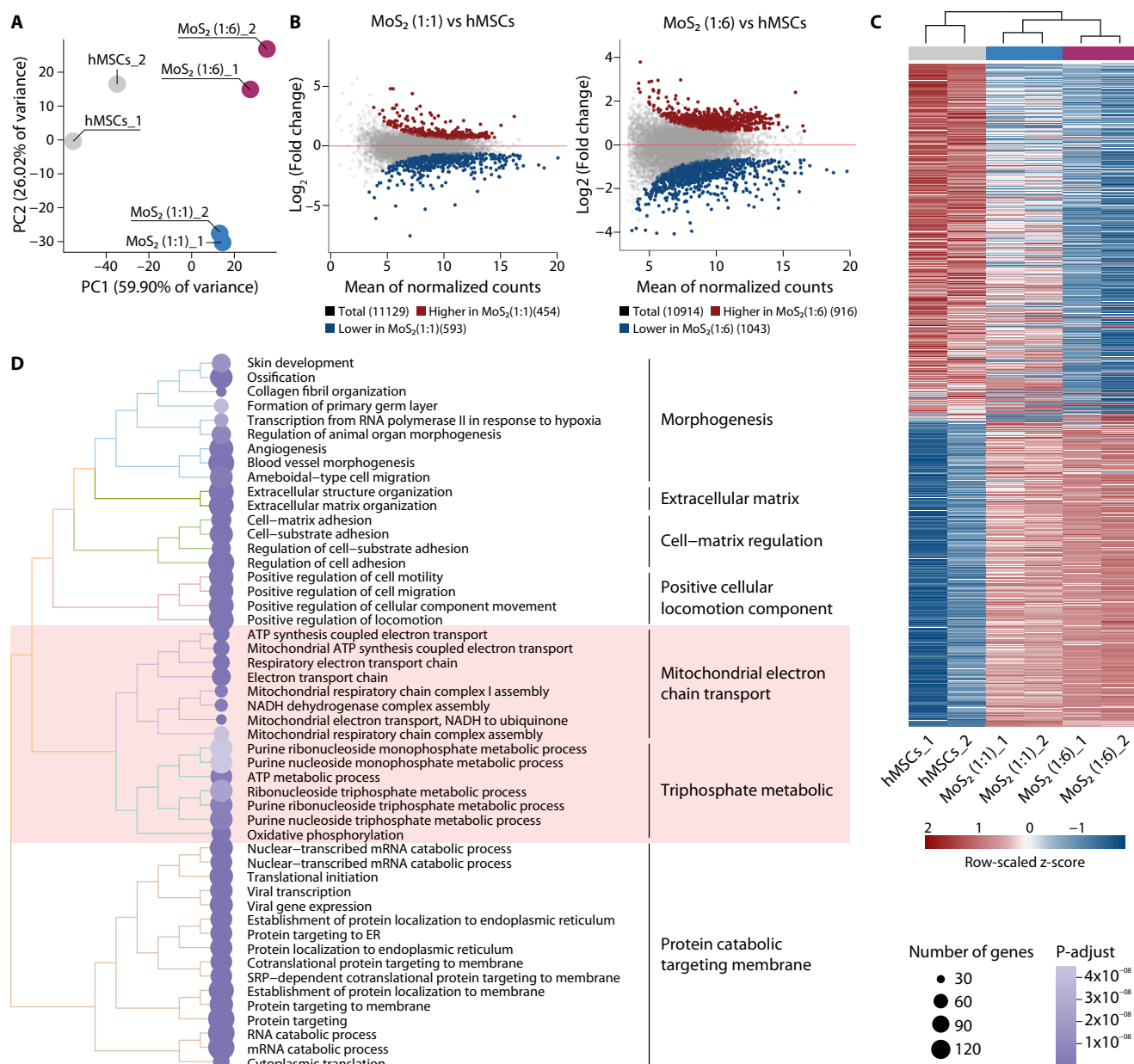


**Fig. 2 | Role of atomic vacancies of MoS<sub>2</sub> on transcriptomic profile of human mesenchymal stem cells. A** Principal component analysis (PCA) of hMSC samples treated with MoS<sub>2</sub> nanoflower with predefined atomic vacancies (1:1 (blue) and 1:6 (purple)) based on mRNA expression obtained from RNA-seq ( $n = 2$ , technical replicates). Untreated hMSCs are used as control (gray). The PCA was done on the mRNA expression (Log<sub>2</sub>FPKM) of 20% of the most variable genes across all samples ( $n = 2214$ ). **B** MA plot showing differences in gene expression [Log<sub>2</sub>(fold change)] between hMSC samples treated with MoS<sub>2</sub> nanoflower (1:1 and 1:6). Genes with significantly high expression are shown in red (P-adj < 0.05), while genes with significantly low expression (P-adj < 0.05) are shown in blue. Gray denotes genes that

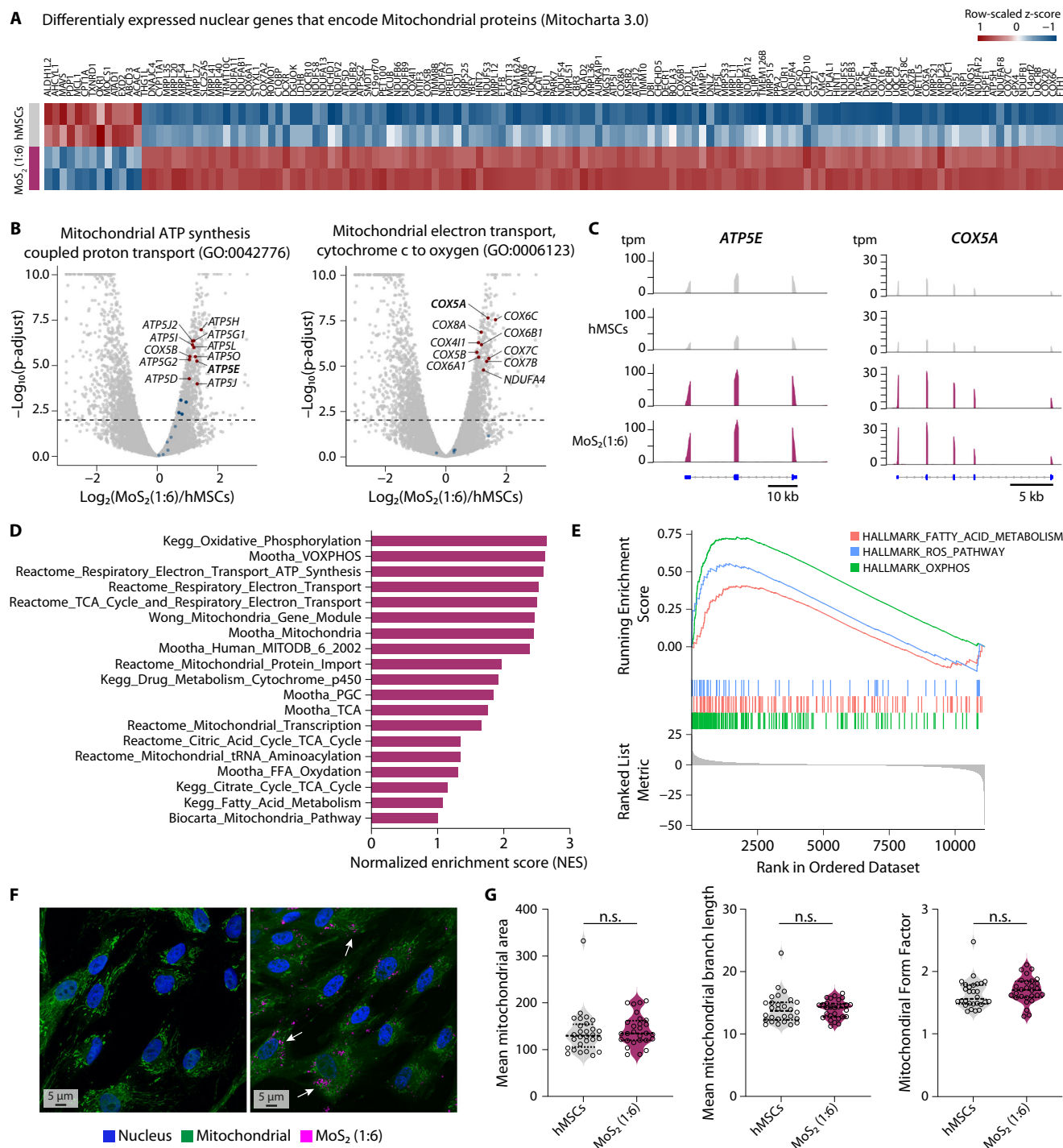
do not significantly exhibit differences. **C** Hierarchical clustering of hMSC samples treated with MoS<sub>2</sub> nanoflower (1:1 and 1:6) based on mRNA expression obtained from RNA-seq. The heatmap shows the DEGs (Log<sub>2</sub>FPKM of DEGs; P-adj < 0.05) across all treatment groups compared with control hMSC samples (red, up-regulated; blue, down-regulated). The total number of distinct DEGs across all samples is 2214. **D** Semantic comparisons of GO annotations for hMSC samples treated with MoS<sub>2</sub> nanoflower (1:6), resulting in seven broad clusters of GO terms: morphogenesis, extracellular matrix, cell-matrix regulation, cellular locomotion component, mitochondrial electron chain transport, triphosphate metabolic, and protein catabolic targeting membrane.

PAGE/Western blot analysis. Cells exposed to MoS<sub>2</sub> with high atomic vacancies (MoS<sub>2</sub> 1:6) showed an increased abundance of multiple OXPHOS subunits including, succinate dehydrogenase subunit B (SDHB, Complex II), ubiquinol-cytochrome *c* reductase core protein 2 (UQCRC2, Complex III), ATP synthase alpha-subunit (ATP5A, Complex V) and mitochondrial membrane proteins such as voltage-dependent anion channel 1 (VDAC1, mitochondrial porin) (Fig. 4D).

To better understand the molecular mechanism by which MoS<sub>2</sub> with high atomic vacancies activates mitochondrial biogenesis, we explored the role of the master regulators of mitochondrial

biogenesis, proliferator-activated receptor gamma coactivator 1 alpha (PGC-1α) and mitochondrial transcription factor A (TFAM)<sup>33</sup>. PGC-1α activates transcription factors NRF1 and NRF2 to induce expression of TFAM<sup>33</sup>. TFAM traffics to the mitochondria, where it is required for mtDNA maintenance and replication<sup>34</sup>. We performed GSEA for targets of PGC-1α using the ENCODE *Transcription Factor Targets* dataset. The GSEA data showed a statistically significant enrichment of PGC-1α associated genes (P-adj < 0.01, NES = 1.92) (Fig. 4E).

Importantly, we observed an increased expression of PGC-1α following exposure to MoS<sub>2</sub> with high atomic vacancies for 3 and 7 days,



respectively (Fig. 4F). While PGC-1 $\alpha$  is primarily responsible for governing the expression of nuclear-encoded mitochondrial genes, the expression of mitochondria-encoded genes is regulated by TFAM. We observed a spike in the expression levels of *TFAM* as early as day 3 after treatment with MoS<sub>2</sub> with high atomic vacancies (Fig. 4G). This implies that the activation of mitochondrial biogenesis as a result of MoS<sub>2</sub> treatment occurs as early as 72 h post-treatment with the nanoparticle. Concordant with these findings, we observed that treated cells exhibited increased expression of genes required for the maintenance of mt-DNA copy number, such as DNA binding protein *SSBP1*<sup>35</sup> (fold change =  $2^{1.39}$ , *Padj* < 0.01), *DGUK*<sup>36</sup> (fold change =  $2^{1.03}$ , *Padj* < 0.01), and *MPV17*<sup>37</sup> (fold change =  $2^{0.75}$ , *Padj* < 0.01). Taken together, these results suggest that atomic vacancy rich MoS<sub>2</sub> treatment triggers

mitochondrial biogenesis by inducing the expression of PGC-1 $\alpha$  and subsequent mitochondrial biogenesis.

### High atomic vacancy increases mitochondrial bioenergetics while decreasing oxidative stress

Increased mitochondrial biogenesis is expected to increase mitochondrial respiration and ATP production. Oxygen consumption rate (OCR) measurement by Seahorse XF24 assay in C2C12 cells treated with or without high atomic vacancy MoS<sub>2</sub> showed that MoS<sub>2</sub> treatment increased the spare respiratory capacity (Fig. 5A). Similarly, in mouse bone marrow derived macrophages we observed that exposure to MoS<sub>2</sub> with high atomic vacancies for 18 h increased both basal and spare respiratory capacity, irrespective of macrophage polarization

**Fig. 3 | Effect of atomic vacancies in MoS<sub>2</sub> nanoflowers on nuclear-encoded mitochondrial genes.** **A** Heatmap showing the DEGs (Log<sub>2</sub>FPKM of DEGs; P-adj < 0.01) known to encode mitochondrial proteins. Samples treated with vacancy rich MoS<sub>2</sub> show consistent upregulation of mitochondrial genes as compared to untreated hMSC samples. **B** Volcano plot highlighting genes involved in mitochondrial ATP synthesis coupled proton transport (GO:0042776) and mitochondrial electron transport, cytochrome c to oxygen (GO:0006123) for high vacancies MoS<sub>2</sub> nanoflowers (1:6). Gray, all of the expressed genes; Blue, all genes associated with the GO term; Red, genes associated with the GO term that show significant difference. MoS<sub>2</sub> nanoflowers with high atomic vacancies enhance the transcription of key MRC genes, including those in the adenosine triphosphate (ATP) and mitochondrial cytochrome c oxidase (COX) families. **C** RNA-seq tracks showing normalized mRNA expression (aligned reads normalized by total library size—transcript per million (TPM)) at the genomic locus of ATP5E and COX5A. **D** GSEA shows positive enrichment of MRC related terms. Positive NES indicates a significant number of genes belonging to these processes are upregulated. **E** GSEA

enrichment results showing NES for *Hallmark: Reactive oxygen species*, *Hallmark: OXPHOS* and *Hallmark: Fatty acid metabolism* for MoS<sub>2</sub> (1:6) treatment. The vertical black lines (bar code) represent the projection onto the ranked gene list of individual genes of the gene set. The horizontal bar in graded color from red (left) to blue (right) represents the gene list ranked from up-regulated on the left to down-regulated on the right. **F** Sub-cellular localization of MoS<sub>2</sub> nanoflowers was determined by co-staining mitochondrial (green) and MoS<sub>2</sub> nanoflowers (purple). The nucleus and mitochondria were stained using DAPI and Mito tracker red, respectively. The arrow points towards MoS<sub>2</sub> nanoflowers that were visualized using reflective light imaging. **G** Quantification of mitochondrial morphology with and without MoS<sub>2</sub> exposure by Mito Hacker analysis. Mitochondrial network parameters were graphed to observe any effect of MoS<sub>2</sub> on mitochondrial morphology. (Data represented violin plots with horizontal lines indicating the median and quartiles. *n* = 28 cells analyzed from three distinct sets of confocal images. Statistical significance was determined using two-tailed student t test, n.s. *p* > 0.05).

(Supplementary Fig. 10). In addition, we observed enhanced total ATP production in hMSCs treated with MoS<sub>2</sub> as compared to untreated cells (Fig. 5B). This increase in respiratory capacity and total cellular ATP production can be attributed to increased mitochondrial biogenesis, as observed by the higher mt-DNA copy number and increased abundance of OXPHOS proteins in cells exposed to MoS<sub>2</sub> with high atomic vacancies (Supplementary Fig. 9 and 11). Further, we observed no significant disruption of mitochondrial membrane potential in treated cells, indicating that treatment with MoS<sub>2</sub> does not disrupt mitochondrial membrane integrity and likely results in more newly synthesized mitochondria capable of maintaining a mitochondrial membrane potential comparable to that of untreated cells (Fig. 5C and Supplementary Fig. 12).

To check if nanomaterial treatment resulted in altered cellular ROS levels, we treated hMSCs with vacancy rich MoS<sub>2</sub> for 24 h and measured total cellular ROS. We observed a decrease in cellular ROS levels in cells treated with MoS<sub>2</sub> as compared to untreated cells (Fig. 5D and Supplementary Fig. 3B). We also observed a similar decrease in mitochondria-specific ROS as determined by using mitochondrial superoxide indicator MitoSOX (Fig. 5E). This corroborates with the RNA-Seq data showing cells treated with high atomic vacancy MoS<sub>2</sub> exhibited an increased expression of antioxidant genes such as *superoxide dismutase type 1 (SOD1)*, fold change = 2<sup>0.89</sup>, *P*-adj < 0.01, and members of the glutathione *S*-transferase (*GST*) family *Glutathione S-transferase omega-2 (GSTO2)*, fold change = 2<sup>1.50</sup>, *P*-adj < 0.01, *Glutathione S-Transferase Zeta 1 (GSTZ1)*, fold change = 2<sup>1.37</sup>, *P*-adj < 0.01 (Fig. 5F). Together, these results indicate that MoS<sub>2</sub> nanoflowers with high atomic vacancies scavenge cellular ROS, reducing oxidative stress in treated cells. The reduction in ROS levels at early (24 h) and enhanced expression of antioxidant genes at later (7 days) time points, could be attributed to a combination of catalytic reduction by MoS<sub>2</sub> with high atomic vacancies and the activation of antioxidant genes by PGC-1 $\alpha$ , respectively.

PGC-1 $\alpha$  acts as the primary conduit through which signaling cascades modulate mitochondrial biogenesis. The post-transcriptional activation of PGC-1 $\alpha$  can occur via pathways such as SIRT1 or AMP-activated protein kinase (AMPK)<sup>38</sup>. SIRT1 directly responds to levels of oxidative stress within cells, acts as a ROS-suppressor, and exhibits antioxidative effects<sup>39,40</sup>. SIRT1 has been shown to be directly responsible for the activation of PGC-1 $\alpha$  through deacetylation of inactive PGC-1 $\alpha$  in the cytosol<sup>41</sup>. The ability of vacancy-rich MoS<sub>2</sub> to enhance mitochondrial biogenesis via PGC-1 $\alpha$  activation was further validated using PGC-1 $\alpha$  knockdown cells (Fig. 5G). PGC-1 $\alpha$  knockdown cells showed no significant increase in mt-DNA copy number following exposure to vacancy rich MoS<sub>2</sub>, this was in stark contrast to cells transfected with empty pLKO vector (Fig. 5H). In TFAM knockdown cells (Supplementary Fig. 13A), MoS<sub>2</sub> treatment led to a minor increase in mt-DNA copy number (Supplementary Fig. 13B) which can be

attributed to the activity of residual TFAM. In summary, these results indicate that vacancy rich nanoflowers mediate mitochondrial biogenesis primarily via PGC-1 $\alpha$  activation.

It is interesting to note that reduction in oxidative stress resulting in SIRT1/PGC-1 $\alpha$  activation and subsequent mitochondrial biogenesis has also been observed in other therapeutic compounds such as Resveratrol<sup>42</sup>. However, compared to vacancy rich MoS<sub>2</sub>, single dose treatment with resveratrol or antioxidant N-acetyl cysteine induces a less robust increase in mitochondrial biogenesis (Fig. 5I). Based on the above results, which demonstrate a reduction in cellular ROS production and an enhancement of mitochondrial biogenesis, we propose that vacancy rich MoS<sub>2</sub> might mitigate cellular ROS. This reduction potentially triggers the SIRT1/PGC-1 $\alpha$  cascade, one of the principal activators of mitochondrial biogenesis, leading to increased mitochondrial function and formation (Fig. 5J).

Thus, we have engineered MoS<sub>2</sub> nanoflowers with predefined atomic vacancies. These vacancies, embedded within the layered architecture of MoS<sub>2</sub>, serve to increase the number of active catalysis sites in the nanoflowers. MoS<sub>2</sub> with high atomic vacancies stimulated OXPHOS biogenesis and thereby promoted cellular respiration. We observed upregulated transcription of key OXPHOS genes and amplified mt-DNA copy number in cells treated with vacancy-rich MoS<sub>2</sub>. This increased transcription of nuclear-encoded mitochondrial genes significantly increased ATP production, elevated cellular respiration, and increased relative expression of OXPHOS complexes. This upsurge in mitochondrial activity most likely stemmed from the activation of the SIRT1/PGC-1 $\alpha$  pathway, leading to mitochondrial biogenesis, initiated by the reduction of cellular ROS by MoS<sub>2</sub> with high atomic vacancies. Existing mitochondrial therapeutics predominantly operate by modulating mitochondrial bioenergetics or enhancing mitochondrial biogenesis. However, these strategies demonstrate limited efficacy and bioavailability, and the issue of targeted delivery further complicates their implementation<sup>43</sup>. Nanomaterial-based approaches provide numerous advantages, including improved therapeutic targeting and efficacy through surface modification and the addition of cell or tissue-specific targeting moieties. The high surface area and photo-responsive nature of MoS<sub>2</sub> nanoflowers make them an ideal platform for combinatorial therapies. Our findings introduce vacancy rich MoS<sub>2</sub> nanoflowers as a potential therapeutic for promoting mitochondrial biogenesis.

## Methods

### Nanoparticle synthesis

MoS<sub>2</sub> nanoflowers with atomics vacancies were synthesized by varying ratios of molecular precursors of molybdenum and sulfur (Hexaammonium heptamolybdate tetrahydrate and Thiourea

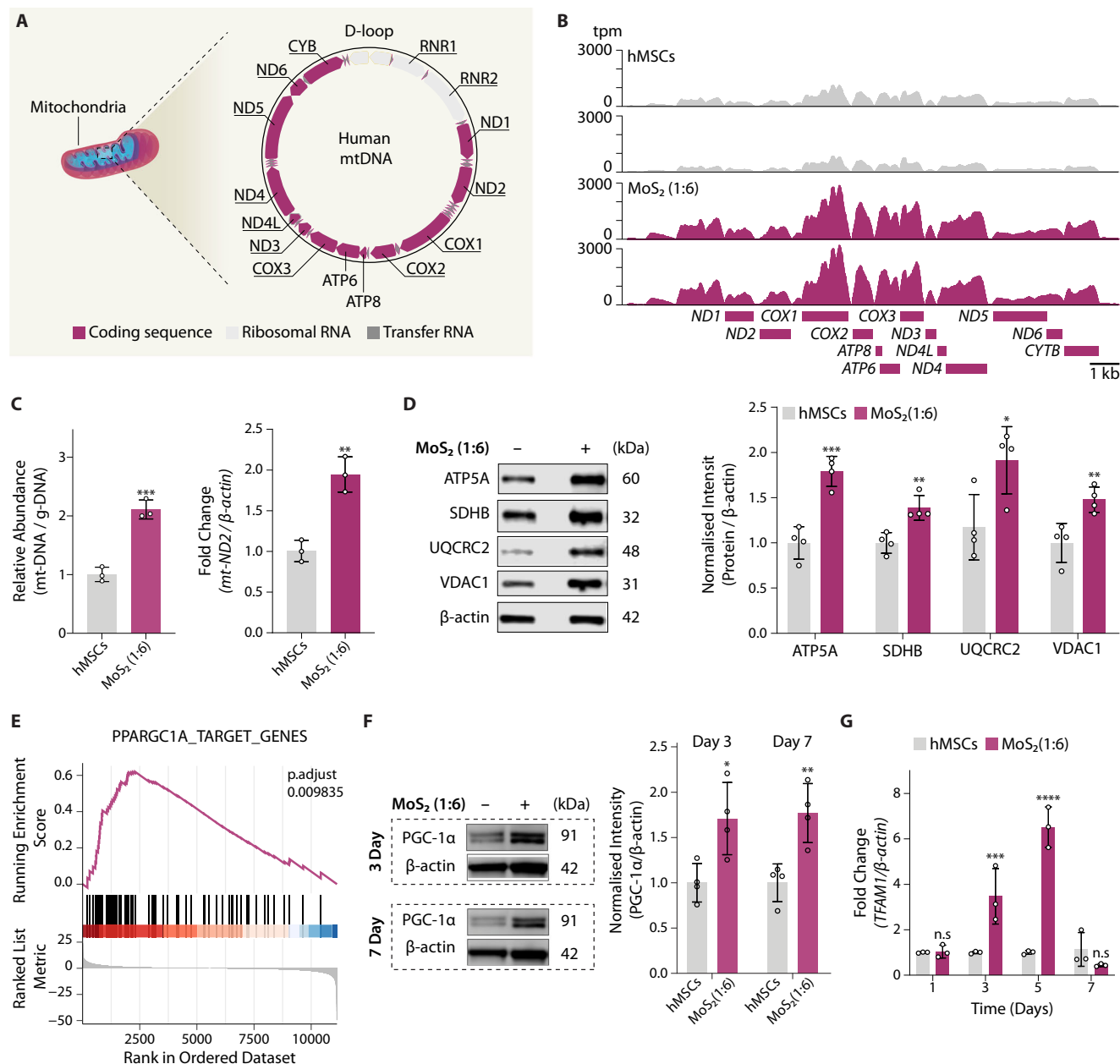


**Fig. 4 | Treatment with MoS<sub>2</sub> nanoflowers stimulates mitochondrial biogenesis.**

**A** Schematic showing mitochondrial genome (mt-DNA), indicating mitochondrial encoded proteins. **B** Visualization of mitochondrial gene expression in cells with and without MoS<sub>2</sub> (1:6) treatment. Data indicates enhanced expression of the entire mitochondrial genome in cells treated with MoS<sub>2</sub> (1:6). **C** The effect of high atomic vacancies MoS<sub>2</sub> on mitochondrial biogenesis. A significant increase in mt-DNA encoded transcript (ND2), as well as copy number (mitochondrial DNA / nuclear DNA), shows that MoS<sub>2</sub> (1:6) treatment results in a significant increase in mitochondrial biogenesis. (Data represented as mean  $\pm$  SD, with  $n = 3$  biological replicates. Statistical significance was determined using two-tailed student t test,  $^{*}p < 0.05$ ;  $^{**}p < 0.01$ ,  $^{***}p < 0.001$ ). **D** Western blotting is used to determine the relative expression of key mitochondrial proteins. MoS<sub>2</sub> (1:6) treatment results in significant upregulation of ATP5B, SDHB, UQCRC2, VDAC1 (Data represented as mean  $\pm$  SD, with  $n = 4$  biological replicates. Statistical significance was determined

using one-tailed student t test,  $^{*}p < 0.05$ ;  $^{**}p < 0.01$ ,  $^{***}p < 0.001$ ). **E** GSEA enrichment of C3: *Regulatory Target* (TFT: *Transcription Factor Targets*) for cells following treatment with MoS<sub>2</sub> (1:6). **F** Relative protein levels of PGC-1 $\alpha$  in cells following treatment with MoS<sub>2</sub> (1:6) were evaluated using Western blotting. MoS<sub>2</sub> treated cells show increased expression of PGC-1 $\alpha$  at both 3 and 7 days respectively, following treatment. (Data represented as mean  $\pm$  SD, with  $n = 4$  biological replicates. Statistical significance was determined using two-tailed student t test,  $^{*}p < 0.05$ ;  $^{**}p < 0.01$ ). **G** Temporal expression of TFAM was monitored for 7 days with and without MoS<sub>2</sub> (1:6) treatment. A 6-fold increase in peak expression due to treatment with MoS<sub>2</sub> (1:6) was observed. (Data represented as mean  $\pm$  SD, with  $n = 4$  biological replicates. Statistical significance was determined using two-way ANOVA with Sidak multiple comparisons tests, n.s.  $p > 0.05$ ;  $^{*}p < 0.05$ ;  $^{**}p < 0.01$ ,  $^{***}p < 0.001$ ,  $^{****}p < 0.0001$ ).

respectively). Varying ratios of these precursors were added to 15 mL of water and then transferred to a hydrothermal device and placed at 220  $^{\circ}$ C for 18 h. Following hydrothermal treatment, the solution was washed with deionized water and ethanol three times respectively, to remove impurities and unreacted precursor. Using this method three

different formulations of MoS<sub>2</sub> nanoflowers were synthesized: nanoflowers with a typical degree of atomic vacancies (Mo:S ratio of 1:2), nanoflowers with a relatively low degree of atomic vacancies (Mo:S ratio of 1:1), and nanoflowers with a relatively high degree of atomic vacancies (Mo:S ratio of 1:6).



## Nanoparticle characterization

Nanoparticle morphology and size was evaluated using Transmission electron microscopy (TEM). Aqueous dispersions of MoS<sub>2</sub> samples were drop-casted on to copper grid (procured from Ted Pella Inc.). After being air -dried overnight, samples were observed using JEOL-JEM 1200 (Japan) at an accelerating voltage of 200 kV. The effect of serum exposure on the surface charge of MoS<sub>2</sub> samples was determined by measuring the zeta potential of the nanoflowers using a Zetasizer Nano ZS (Malvern Instrument, U.K.) with a He–Ne laser at 25 °C. The crystal structure of the MoS<sub>2</sub> nanoflowers was investigated using X-ray powder diffraction (Bruker D8 advanced) using copper K $\alpha$  source (wavelength, 1.54 Å). The data were recorded from 5 to 90 degrees and the obtained peaks were indexed using JCPDS card No. 73–1508. The crystallite size (D) of the nanoflowers was determined based at the characteristic peak (002) using the Scherrer equation given below:

$$D = (K\lambda)/(\beta \cos \theta)$$

Where K is the shape factor (approx. 0.94),  $\lambda$  is X-ray wavelength,  $\beta$  is line broadening at full-width half maxima (FWHM), and  $\theta$  is the Bragg angle. The phase composition of Mo-S atoms within the nanoflowers following the synthesis was determined using X-ray photoelectron spectroscopy (XPS, Omicron Inc.). The binding energies (B.E.) for Mo (3d) and S (2p) for MoS<sub>2</sub> nanoflowers were recorded. The raw data was then processed and deconvoluted by CasaXPS multiple peak fit software version 2.3.15 and indexed using the standard library.

## Cyclic voltammetry (CV)

CV analysis was conducted to determine the active sites in the samples<sup>24</sup>, following the established procedure. All the measurements were done on CH Instruments (model number CHI-660D) electrochemical workstation. In this investigation, we used a three-electrode screen printed electrode (SPE) (TE100, CH Instruments) with a diameter of  $\phi = 3$  mm as the working electrode, a conducting carbon as the counter electrode, and an Ag/AgCl electrode as the reference electrode during the measurements. All the CV measurements were carried out in 1x phosphate buffer solution (PBS) of 7 pH at a scan rate of 50 mV/s.

Before conducting experiments, the screen-printed electrodes underwent a cleaning process. This involved running 10 cyclic voltammetry (CV) cycles at a scan rate of 100 mV/s within a voltage window of  $-0.3$  to  $1.3$  V in a  $0.5$  M H<sub>2</sub>SO<sub>4</sub> solution. Following the cleaning procedure, a 2-microliter volume of a dispersed MoS<sub>2</sub> solution (labeled 1:1, 1:2, and 1:6) at a concentration of 10 mg/mL was drop-casted onto the working electrode of the cleaned SPEs. Subsequently, all the coated electrodes were air-dried at room temperature for 60 minutes and then used for further electrochemical characterizations.

Active sites were calculated by extracting the absolute values of voltammetric charges (both cathodic and anodic) obtained from the cyclic voltammetry scanning from  $-0.2$  to  $0.6$  V (versus Ag/AgCl) using a scan rate of 50 mV/s in PBS with a pH of 7.0. Considering a one-electron redox process that occurred during the reaction, the total charges were divided into two. The number of active sites (n) for the sample deposited on the electrode was determined using the following equation<sup>24</sup>:

$$n = Q/2F(\text{mol/g})$$

where Q: Voltammetric charges; F: Faraday constant ( $C \text{ mol}^{-1}$ )

## Amperometric analysis

Amperometry was performed at the H<sub>2</sub>O<sub>2</sub> reduction voltage of  $-0.6$  V in order to compare the output currents of all the MoS<sub>2</sub>

samples<sup>44</sup>. All amperometric measurements are carried out in N<sub>2</sub>-saturated 5 mM H<sub>2</sub>O<sub>2</sub> in 1xPBS of 7 pH. The output reduction current density of samples was used to determine their H<sub>2</sub>O<sub>2</sub> reduction capability.

## Catalase Activity

The catalytic activity of MoS<sub>2</sub> nanoflowers was determined by comparing the reduction of hydrogen peroxide by nanoflowers to the reduction caused by the bovine catalase enzyme. The assay was performed using the Catalase Colorimetric Activity Kit (Invitrogen, catalog no: EIACATC), with the nanoflowers dispersed in PBS at a concentration of 25  $\mu\text{g/mL}$ .

## Cell culture

For the culture of Human mesenchymal stem cells (hMSCs) (RoosterBio and Lonza),  $\alpha$ -minimal essential media (alpha-MEM, Hyclone, GE Sciences) with 16.5% fetal bovine serum (Atlanta Biologicals, USA) and 1% penicillin/streptomycin (100 U/100  $\mu\text{g/mL}$ , Gibco) were utilized. Cells were cultured under 5% CO<sub>2</sub> at 37 °C. The culture media was removed and replaced with fresh media every 2–3 days. Cells were passaged at 70% confluency, following which cells media was removed, cells were washed with 1X PBS and then treated with 0.5% trypsin-EDTA. For normal culture cells were seeded at  $\sim 2500$  cells/cm<sup>2</sup>. All experiments were completed with cell populations under passage 5.

H9c2 and C2C12: Cells were cultured in high-glucose Dulbecco's Modified Eagle Medium (DMEM) media supplemented with 10% fetal bovine serum (FBS) (Atlanta Biologicals, USA), 1 mM sodium pyruvate and % penicillin/streptomycin (100 U/100  $\mu\text{g/mL}$ , Gibco). Cells were passaged with 0.5% trypsin-EDTA upon reaching a confluency of  $\sim 70\%$  and seeded at  $\sim 2500$  cells/cm<sup>2</sup>. Cells were cultured under 5% CO<sub>2</sub> at 37 °C.

BMDM: Bone marrow derived macrophages (WT) were isolated from mice as described in previous work<sup>45</sup>. BMDM cells were cultured in Dulbecco's Modified Eagle Medium (DMEM) (Life Technologies) supplemented with 10% fetal bovine serum (FBS) (VWR). LPS (200 ng/mL) and IL-4 (20 ng/mL) treatments were performed 5 h after treatment with nanoparticles. Cells were cultured under 5% CO<sub>2</sub> at 37 °C.

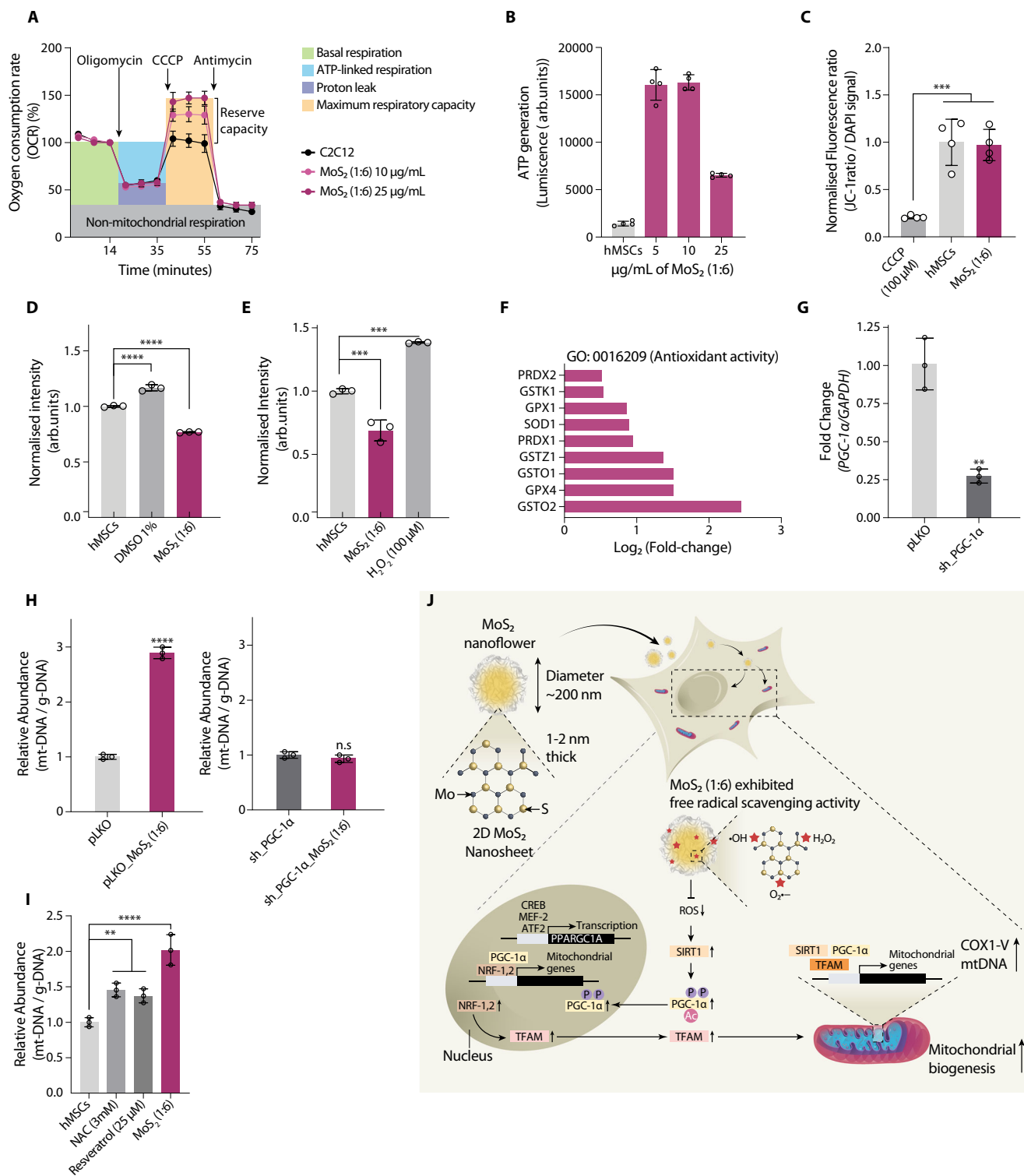
## Protein corona formation

The composition of the protein corona formed around the nanosheet was investigated by an SDS-PAGE gel electrophoresis. Briefly, the nanosheets were incubated with serum-supplemented alpha MEM media for 2 h at 37 °C. The samples were then centrifuged at 10,000 g and washed 3 times with PBS. The nanosheets were then suspended in LDS loading buffer (Thermo Fisher), followed by incubation at 90 °C for 15 minutes, and subsequent gel electrophoresis was performed. The gels were then stained using Imperial Blue stain (Thermo Fisher).

## In vitro assays

For cytotoxicity assays, hMSCs were seeded in 96 well plates at a seeding density of 5000 cells per well. The cells were exposed to varying concentration of MoS<sub>2</sub> nanosheets for a pre-defined time of 24 h for cytotoxicity, followed by measurement of toxicity using Cyquant and LDH assay (Thermo Scientific) respectively, as per the manufacturer's protocols.

For assessing cell proliferation, hMSCs were seeded in different 96 wells (corresponding to each time point) plates at 5000 cells per well, and then treated with MoS<sub>2</sub> (1:6) at a concentration of 25  $\mu\text{g/mL}$ . Following each time point, DNA content and total cell number were assessed in cells, with and without MoS<sub>2</sub> exposure, using the Cyquant assay (Thermo Scientific) per the manufacturer's protocols.



For cell cycle analysis, hMSCs were cultured in 6 well plates. After reaching 50% confluency, hMSCs were serum starved (only 1% FBS in media) for 12 h to synchronize cell populations, followed by treatment with MoS<sub>2</sub> nanosheets (25 µg/mL). After 72 h of exposure, the cells are trypsinized and fixed in ice-cold 70% ethanol. The cells are then centrifuged and washed with PBS 3 times, followed by incubation with PI (40 µg/mL) and Rnase (100 µg/mL) at 37 °C for 1 h. Cells were stored at 4 °C till flow cytometry analysis, which was performed using the BD Accuri C6 flow cytometer.

ATP production was measured using a bioluminescence assay. For this assay hMSCs were seeded in a 96 well plate at a density of 5000 cells per well. Following this, the hMSCs were treated with varying concentrations of vacancy rich MoS<sub>2</sub> nanoflowers for 72 h, after which ATP levels were measured using an ATP determination kit (Thermo Fisher) as per manufacturer's protocol.

Fluorescence imaging of hMSCs treated with MoS<sub>2</sub> nanoflowers was performed using a confocal microscope (Leica Sp8). Cells were cultured in chambered coverslips (ibidi) followed by exposure to

**Fig. 5 | High atomic vacancy MoS<sub>2</sub> decreases oxidative stress and enhances mitochondrial bioenergetics.** **A** The effect of MoS<sub>2</sub> on OCR was determined in C2C12 cells treated with different concentrations of MoS<sub>2</sub> (1:6) (0, 10 and 25 µg/mL). A concentration-dependent increase in spare respiratory capacity was observed, indicating the ability of MoS<sub>2</sub> to activate mitochondrial respiration machinery. (*n* = 3 biological replicates). **B** Evaluation of ATP levels in cells treated with MoS<sub>2</sub> (1:6) suggests a marked increase in ATP levels, compared to untreated hMSCs. (*n* = 4 biological replicates). **C** Effect of MoS<sub>2</sub> on mitochondrial membrane potential. Cells treated with MoS<sub>2</sub> (1:6) showed no significant changes in mitochondrial membrane potential as compared to untreated cells. Cell number variation was normalized using nuclear stain (DAPI). (*n* = 4 biological replicates). **D** The amount of intracellular ROS is determined before and after treatment with MoS<sub>2</sub> (1:6). MoS<sub>2</sub> treatment significantly suppressed ROS production. (*n* = 3 biological replicates). **E** The amount of mitochondrial ROS is determined using MitoSox before and after treatment with MoS<sub>2</sub> nanoflowers (1:6). MoS<sub>2</sub> treatment significantly suppressed mitochondrial ROS production. (*n* = 3 biological replicates). **F** RNA-seq data demonstrates the upregulation of multiple genes related to antioxidant activity

(GO: 0016209). **G** PGC-1α expression in C2C12 transduced with either empty vector (pLKO) or shRNA targeting PGC-1α (*n* = 3 biological replicates). **H** Evaluation of relative mitochondrial copy number in transduced cells following treatment with MoS<sub>2</sub> for 72 h. (*n* = 3 biological replicates). **I** Mitochondrial copy number in hMSCs following treatment with N-acetyl cysteine (NAC), resveratrol, and vacancy-rich MoS<sub>2</sub>. Cells were treated with either NAC (3 mM), resveratrol (25 µM), or MoS<sub>2</sub> (1:6) (25 µg/mL) for 72 h. (*n* = 3 biological replicates). **J** Proposed mechanism of action of MoS<sub>2</sub> with high atomic vacancies on triggering mitochondrial biogenesis. It is expected that atomic vacancies of MoS<sub>2</sub> exhibit free radical scavenging activity through rapid reactions with reactive oxygen species (ROS), including hydrogen peroxide (H<sub>2</sub>O<sub>2</sub>), superoxide anions (O<sub>2</sub><sup>•−</sup>), and hydroxyl radicals (•OH). Reduction in intracellular ROS due to the presence of atomic vacancies on MoS<sub>2</sub> is expected to trigger the SIRT1/PGC1α/NRF2 pathway. For (A), (B), (C), (D), (E), (G), (H), and (I), data represented as mean ± SD. For (C), (D), (E), (I) Statistical significance was determined using one way ANOVA with post hoc Tukey test. For (G), (H) Statistical significance was determined using a two-tailed student t test. For all data sets n.s. *p* > 0.05, \**p* < 0.05, \*\**p* < 0.01, \*\*\**p* < 0.001, \*\*\*\**p* < 0.0001.

nanoflowers for 24 h, after which cells were washed 3 times with PBS and fixed by incubation samples with 4% paraformaldehyde (PFA) for 20 minutes at room temperature. (if needed, cells were permeabilized with 0.1 % Triton X-100 for 10 minutes at room temperature). MoS<sub>2</sub> nanoparticles were imaged using reflective light, with the nucleus, f-actin, and mitochondria stained using DAPI (Biotium), Acti-Stain 670 Phalloidin (Cytoskeleton, Inc), and Mito tracker red (Thermo Fisher) respectively.

### TEM imaging of internalized nanoflowers

hMSCs were cultured in chambered slides (Nunc, Lab-Tek Chamber Slide, Thermo Scientific) overnight, followed by treatment with MoS<sub>2</sub> (1:6) nanoflowers for 24 h. Cells were then fixed using Trump's universal fixative for 2 hr at room temperature. Following this, samples were subjected to sequential dehydration in varying concentrations of ethanol (50%, 70%, and 100%) and infiltration with and polymerization of epoxy resins. The polymerized epoxy resin blocks were separated from the glass slide to expose the embedded cell monolayer. Ultra-thin sections (60–80 nm) were cut parallel with the surface on a Leica UC7 ultramicrotome using a diamond knife, collected on 300-mesh copper grids with carbon support film and stained with uranyl acetate and Venable lead citrate, 5 minutes each<sup>46</sup>. Transmission electron microscopy (TEM) of the stained grids was performed using a JEOL-JEM 1200 (Japan) at an accelerating voltage of 200 kV.

### Transcriptome sequencing (RNA-seq)

hMSCs were treated with low atomic vacancy and high atomic vacancy MoS<sub>2</sub> nanoflowers, respectively, at a concentration of 25 µg/mL for a period of 7 days, with untreated cells acting as a control group. 48 h after initial treatment, the excess nanoflowers were then removed during routine media change and the cells were cultured for an additional 5 days in normal media condition. On the 7<sup>th</sup> day of treatment, cells were harvested, and total RNA was extracted using the Zymogen Quick RNA Miniprep kit. mRNA concentration and quality were assessed using NanoDrop®, with an absorbance ratio threshold A260/A280 > 2 for samples used for sequencing.

Sequencing was performed using a Nova seq platform (Illumina Nova SEq. 6000), using a Truseq RNA preparation and 75 paired-end read length. Following sequencing, reads were aligned to the human genome (hg38, GRCh37 Genome Reference Consortium Human Reference<sup>37</sup>, obtained from University of California, Santa Cruz) using the R-Bioconductor package Spliced Transcripts Aligned to a Reference (STAR)<sup>47</sup>. mRNA levels of nanomaterial treated hMSCs samples were compared to untreated hMSCs to determine nanomaterial exposure induced differential expression of genes. For untreated hMSCs, 30672868 (22477324 uniquely mapped) and 26167130 (19300764 uniquely mapped) reads were aligned to the genome for the 2 replicates. Similarly, for hMSCs treated with low atomic vacancy MoS<sub>2</sub>, 24580412

(17841369 uniquely mapped) and 29456043 (22339102 uniquely mapped) reads were aligned to the genome for the 2 replicates. In the case of hMSCs treated with high atomic vacancy MoS<sub>2</sub>, 24852928 (18123996 uniquely mapped) and 23488937 (17814934 uniquely mapped) reads were aligned to the genome for the 2 replicates.

Only uniquely mapped reads were used for subsequent analysis. RefSeq gene models were retrieved from UCSC and used to quantify expression to read counts using the uniquely mapped reads of the coding exons, normalized by gene length using reads per kilobase of transcript per million mapped reads (RPKM) factor. Genes expressed with RPKM > 1 in at least half of the samples of any condition were considered expressed and genes with RPKM < 1 were considered to have minimal to no expression. Bioconductor package DESeq2 was utilized for genes expressed in treatment conditions (i.e., differentially expressed genes) via negative binomial distribution<sup>48,49</sup>. Following this, Log2-adjusted RPKM was used for further analysis such as high dimensional clustering (HDC). Differentially expressed genes (DEGs) were sorted with a statistical threshold (Benjaminin-Hochberg false discovery rate (FDR) adjust) *Padj* < 0.01. Statistically significant DEGs were used to determine functional enrichment of gene ontology terms part of Biological Processes (BP), Molecular Functions, and Cellular Components. Enrichment analysis was performed using the Bioconductor package GoStats<sup>50</sup> (using conditional hyperGTest of over-representation) and Metascape<sup>51</sup>. Gene tracks for key target genes were generated using the Gviz package<sup>52</sup>.

Gene set enrichment analysis (GSEA) was performed using the GSEA java desktop application against the current Molecular Signatures Database (v7.4 MsigDB). DEG rank lists were constructed using the following function: Rank = -Log10(*P* value) \* sign (Fold Change). Ranked lists were then used in the GSEA desktop application and a GSEA Preranked analysis was performed with default test parameters (which included *collapse* to collapse dataset to gene symbols before analysis and excluded gene set sizes of greater than 500 and less than 15). During this analysis the ranked list was compared to a priori sets of genes in the curated collection of the Molecular Signatures Database (v7.4 MsigDB). The chip platform used for analysis was the Human ENSEMBL\_Gene\_ID\_MsigDB.v7.5.chip dataset. Probed databases included current releases of curated Hallmarks (h.all.v7.5.symbols.gmt), Reactome (c2.cp.reactome.v7.5.symbols.gmt), Wikipathways (c2.cp.wikipathways.v7.5.symbols.gmt), and GO (c5.all.v7.5.symbols.gmt). Enriched GSEA terms were then represented using Log10 transformation of FDR-adjusted *P* value (i.e., *Q* value) and normalized enrichment score (NES). Gene sets with an FDR of less than 10% (FDR < 0.1) were considered significant.

### Gene expression analysis and mt-DNA copy number

To measure the mt-DNA encoded transcripts, hMSCs were treated with/without MoS<sub>2</sub> (1:6) for 1, 3, 5, and 7 days, respectively, followed by

RNA extraction using RNA extraction Kit (Zymo research). The RNA was converted into cDNA using a first-strand cDNA synthesis kit (Qunatbio) following the manufacturer recommended protocol. cDNA generated was then stored at  $-20^{\circ}\text{C}$  until further use.

Quantitative real-time polymerase chain reaction (qRT-PCR) experiments were performed using TaqMan assays for target genes (*mt-ND2* assay ID: Hs02596874\_g1; *ACTB* assay ID: Hs03023943\_g1; *TFAM* assay ID: Hs00273372\_s1; *GAPDH* assay ID: Hs02758991\_g1) and TaqMan Fast Advanced Master Mix (Thermo Fisher), with and initial cDNA mass of 1 ng per reaction. Changes in the expression levels of target genes as a result of  $\text{MoS}_2$  exposure were determined using Comparative CT ( $\Delta\Delta\text{CT}$ ) analysis, with  $\beta$ -actin (*ACTB*) acting as an endogenous control.

The relative mt-DNA copy number was determined by using DNA extracted from the control and  $\text{MoS}_2$ -treated cells via a DNA extraction Kit (Zymo research). By comparing the expression levels of a mitochondrial encoded gene (*mt-ND2*) and with that of nuclear DNA (*GAPDH*), we can determine the relative change in mt-DNA expression when comparing  $\text{MoS}_2$ -treated cells to untreated (control) cells. qRT-PCR assays were performed in a manner similar to those described above, with total cellular DNA being utilized in place of mRNA-derived cDNA. All qRT-PCR experiments were performed using a QuantStudio™ 3 System (Applied Biosystems).

For mouse cell lines, RT-PCR experiments were performed using SYBR chemistry for the following targets:

*PGC-1 $\alpha$*  (F: GAATCAAGCCACTACAGACACCG; R: CATCCCTCTTGAGCCTTTCGTG),

*TFAM* (F: GAGGCAAAGGATGATTGGCTC; R: CGAATCCTATCATCTTTAGCAAGC),

*GAPDH* (F: CATCACTGCCACCCAGAAGACTG; R: ATGCCAGTGAGCTTCCCGTTCAG),

*mt-ND2* (F: AGGGATCCCACTGCACATAG; R: TGAGGGATGGGTGTGAAGGA)<sup>53</sup>.

RT-PCR was performed using 5 ng of cDNA/genomic DNA template, with the default SYBR cycling condition of the QuantStudio 3.

### Seahorse assay

The Seahorse XF24 Extracellular Flux Analyzer was used to determine the oxygen consumption rate (OCR), as previously described<sup>54</sup> with minor modifications. The cells were seeded in XF24-well cell culture microplates (Agilent Technologies) at 10,000 cells per well in appropriate media and incubated at  $37^{\circ}\text{C}$  in a 5%  $\text{CO}_2$  incubator overnight. Following this, cells were treated with high atomic vacancy  $\text{MoS}_2$  for varying periods depending on the cell type (48 h for C2C12 cells, and 18 h for BMDM cells).

To begin the OCR measurements, existing culture media from each well was removed and replaced with 775  $\mu\text{L}$  of fresh growth medium, following which cells were incubated at  $37^{\circ}\text{C}$  without  $\text{CO}_2$  for 30 min. The OCR measurements were performed using the Seahorse XF24 Extracellular Flux Analyzer (Agilent Technologies). The Mix, wait, and measure steps of the testing protocol were set at 2 mins for each step. The mitochondrial stress test was performed by the sequential injection of oligomycin (2  $\mu\text{M}$ ), carbonyl cyanide 3-chlorophenylhydrazone (CCCP) (20  $\mu\text{M}$ ), and antimycin A (2  $\mu\text{M}$ ). For BMDM cells, post-assay cell normalization was performed by quantifying cellular DNA content using the DRAQ5™.

### Reactive oxygen species (ROS)

Untreated hMSCs (negative control) and  $\text{MoS}_2$  (1:6) treated cells were seeded in a 6-well plate at 60% confluency. After 24 h of growth, media was replaced by PBS and samples were incubated with 1–2  $\mu\text{M}$  DCFDA (for cellular ROS) for 10–15 min in the dark. The cells were then harvested, and fluorescence was measured using flow cytometry (BD Accuri C6). Cells exposed to 1% DMSO for 10 minutes or 100  $\mu\text{M}$   $\text{H}_2\text{O}_2$  for 15 minutes at  $37^{\circ}\text{C}$  were used as a positive control. Similarly, to

determine mitochondria-specific ROS production, mitoSOX (Thermo Fisher) was used according to the manufacturer's protocol. In the case of mitochondrial ROS generations, cells exposed to 100  $\mu\text{M}$   $\text{H}_2\text{O}_2$  for 15 minutes at  $37^{\circ}\text{C}$  were used as a positive control. All samples were analyzed using flow cytometry (BD Accuri C6) with appropriate gating and fluorescent channels (Supplementary Fig. 14).

### shRNA lentiviral infection and knockdown generation

The gene-specific shRNA plasmids (PGC-1 $\alpha$ : TRCN0000234017, TFAM: TRCN0000311846, Empty pLKO vector: SHC001V) were acquired from Mission shRNA collection (Sigma). Lentiviral particle production and infection were performed as described previously<sup>55</sup>. For generation of stable knockdown cell lines, C2C12 cells were seeded in a six-well dish at a concentration of 100,000 cells per well. Following overnight incubation at  $37^{\circ}\text{C}$  in a 5%  $\text{CO}_2$ , 2 mL of polybrene containing media (with polybrene at a concentration of 8  $\mu\text{g}/\text{mL}$ ) was added to each well, after which 100  $\mu\text{L}$  of viral supernatant was added to each well. The plates were spun at 805 g for 30 min at  $30^{\circ}\text{C}$ , returned to a  $37^{\circ}\text{C}$  incubator for 24 h. The selection of successfully transfected cells was performed by culturing cells in 2  $\mu\text{g}/\text{mL}$  puromycin-containing medium for 72 h. Knockdown efficiency was determined using RT-PCR using C2C12 cells transfected with empty pLKO vectors as a control.

### Western blot analysis

Cells were harvested, washed with phosphate-buffered saline (PBS), and lysed on ice in radioimmunoprecipitation assay (RIPA) extraction buffer (Boston BioProducts, BP-115), supplemented with a 1 $\times$  complete protease inhibitor cocktail (Roche), for 30 min and centrifuged at 14,000  $\times$  g for 15 min at  $4^{\circ}\text{C}$ . Following which the supernatants were collected in a fresh tube and protein concentration was determined using the microBCA assay (Pierce). Normalized mass of protein (20  $\mu\text{g}$  per sample) was mixed with reducing sample buffer (Lane Marker Reducing Sample Buffer, Pierce) and denatured at  $95^{\circ}\text{C}$  for 5 minutes. Denatured proteins were separated using 4–12% Bolt Bis-Tris Plus gel (Life Technologies) in MOPS buffer, followed by transfer (Invitrogen, iBlot 2) to a polyvinylidene fluoride (PVDF) or nitrocellulose membrane as per manufacturer's instructions. Membranes were blocked with 5% milk in TBST (1X TBS with 0.1% Tween20) for 1 h prior to antibody staining. Primary antibody incubation was performed overnight at  $4^{\circ}\text{C}$ , while secondary antibody incubation was performed at room temperature for 1 h (Supplementary Dataset 4). Membranes were washed 3 times for 5 minutes with TBST after both the primary and secondary antibody incubation, following which they were developed (SuperSignal™ West Pico PLUS Chemiluminescent Substrate, Thermo Fisher) and imaged using LI-COR® 3600 C-Digit Blot Scanner. Restoration and re-blocking with 5% milk in TBST of the membranes were then done for further protein analysis. Quantification of bands was performed using ImageJ.

### Mitochondrial membrane potential

Mitochondrial membrane potential in cells was evaluated using the JC-1 assay (Cayman). JC-1 dye exhibits different fluorescence in response to membrane potential (under high membrane potential JC-1 for aggregates with red fluorescence, while at low membrane potential, the dye remains in monomeric form, giving a green fluorescence signal). The ratio of these signals indicates a change in mitochondrial membrane potential in response to treatment conditions. Cells treated with 100  $\mu\text{M}$  CCCP for 5 minutes at  $37^{\circ}\text{C}$  were used as positive control. Cell numbers across different treatments were normalized using Hoechst nuclear staining. Fluorescence was measured on a Cytation 5 (Agilent) using appropriate filters.

### Inductively coupled plasma-mass spectrometry (ICP-MS)

Cellular levels of Mo were measured by ICP-MS using a NexION 300D, PerkinElmer, Inc. Briefly,  $2 \times 10^5$  cells from each treatment group (Low



atomic vacancy MoS<sub>2</sub>, high atomic vacancy MoS<sub>2</sub>, no vacancy MoS<sub>2</sub> and untreated hMSCs) were harvested after 18 h of exposure to treatment conditions. Cells were washed twice with 1 mL of PBS, followed by two more washes with 0.9% NaCl prepared in ultrapure water. Following this, the samples were digested with 40% (w/v) nitric acid (TraceSELECT; Sigma-Aldrich) at 90 °C for 18 h, after which samples were subjected to a 6 h digestion with 0.75% H<sub>2</sub>O<sub>2</sub> (Sigma-Supelco), and then serially diluted in ultrapure water. A calibration curve was generated by serially diluting ammonium molybdate in 1.5% nitric acid.

### Statistical analysis

Determination of statistical significance when directly comparing untreated cells and MoS<sub>2</sub> treated cells was determined using the student t-test. Similarly, the determination of statistical significance between multiple groups was achieved via ANOVA with the post hoc Tukey method or a two-way ANOVA with appropriate post hoc tests (Sidak multiple comparisons tests or Tukey). Significant *P* values were considered <0.05 unless otherwise noted. All analysis was completed in GraphPad Prism 9.0.

### Reporting summary

Further information on research design is available in the Nature Portfolio Reporting Summary linked to this article.

### Data availability

All data needed to evaluate the conclusions in the paper are present in the paper and/or the Supplementary Materials. Raw data used to generate figures is available through Zendo data repository (<https://doi.org/10.5281/zenodo.13744481>). Additionally raw data generated in this study is also provided in the Supplementary Information/Source Data file. RNA-seq data reported here have been deposited in the Gene Expression Omnibus (GEO) database, accession no. GSE235996. Source data are provided with this paper.

### References

- Friedman, J. R. & Nunnari, J. Mitochondrial form and function. *Nature* **505**, 335–343 (2014).
- Nunnari, J. & Suomalainen, A. Mitochondria: in sickness and in health. *Cell* **148**, 1145–1159 (2012).
- Seimon, R. V. et al. Effect of weight loss via severe vs moderate energy restriction on lean mass and body composition among postmenopausal women with obesity: the TEMPO diet randomized clinical trial. *JAMA Netw. Open* **2**, e1913733 (2019).
- Park, Y. M. et al. Estradiol-mediated improvements in adipose tissue insulin sensitivity are related to the balance of adipose tissue estrogen receptor  $\alpha$  and  $\beta$  in postmenopausal women. *PLoS One* **12**, e0176446 (2017).
- Khalid, A. B. & Krum, S. A. Estrogen receptors alpha and beta in bone. *Bone* **87**, 130–135 (2016).
- Henderson, V. W. & Brinton, Roberta D. Menopause and mitochondria: windows into estrogen effects on Alzheimer's disease risk and therapy. *Prog. brain Res.* **182**, 77–96 (2010).
- Scheyer, O. et al. Female Sex and Alzheimer's Risk: The Menopause Connection. *J. Prev. Alzheimers Dis.* **5**, 225–230 (2018).
- Wallace, D. C., Fan, W. & Procaccio, V. Mitochondrial energetics and therapeutics. *Annu. Rev. Pathol.: Mechanisms Dis.* **5**, 297–348 (2010).
- Singh, A., Faccenda, D. & Campanella, M. Pharmacological advances in mitochondrial therapy. *EBioMedicine* **65**, 103244 (2021).
- Coleman, J. N. et al. Two-dimensional nanosheets produced by liquid exfoliation of layered materials. *Science* **331**, 568–571 (2011).
- Ye, G. et al. Defects engineered monolayer MoS<sub>2</sub> for improved hydrogen evolution reaction. *Nano Lett.* **16**, 1097–1103 (2016).
- Jaramillo, T. F. et al. Identification of active edge sites for electrochemical H<sub>2</sub> evolution from MoS<sub>2</sub> nanocatalysts. *science* **317**, 100–102 (2007).
- Xie, J. et al. Defect-rich MoS<sub>2</sub> ultrathin nanosheets with additional active edge sites for enhanced electrocatalytic hydrogen evolution. *Adv. Mater.* **25**, 5807–5813 (2013).
- Chimene, D., Alge, D. & Gaharwar, A. K. Two-dimensional nanomaterials for biomedical applications: emerging trends and future prospects. *Adv. Mater.* **27**, 7261–7284 (2015).
- Murali, A., Lokhande, G., Deo, K. A., Brokesh, A. & Gaharwar, A. K. Emerging 2D nanomaterials for biomedical applications. *Mater. Today* **50**, 276–302 (2021).
- Mendel, R. R. & Kruse, T. Cell biology of molybdenum in plants and humans. *Biochimica et. Biophysica Acta (BBA) - Mol. Cell Res.* **1823**, 1568–1579 (2012).
- Garattini, E. & Terao, M. The role of aldehyde oxidase in drug metabolism. *Expert Opin. Drug Metab. Toxicol.* **8**, 487–503 (2012).
- Cao, M. et al. Molybdenum derived from nanomaterials incorporates into molybdenum enzymes and affects their activities in vivo. *Nat. Nanotechnol.* **16**, 708–716 (2021).
- Chou, S. S. et al. Understanding catalysis in a multiphasic two-dimensional transition metal dichalcogenide. *Nat. Commun.* **6**, 8311 (2015).
- Liu, T. et al. Iron oxide decorated MoS<sub>2</sub> nanosheets with double PEGylation for chelator-free radiolabeling and multimodal imaging guided photothermal therapy. *ACS Nano* **9**, 950–960 (2015).
- Wang, H. et al. Electrochemical tuning of vertically aligned MoS<sub>2</sub> nanofilms and its application in improving hydrogen evolution reaction. *Proc. Natl Acad. Sci.* **110**, 19701–19706 (2013).
- Liu, T. et al. Drug delivery with PEGylated MoS<sub>2</sub> nano-sheets for combined photothermal and chemotherapy of cancer. *Adv. Mater. (Deerfield Beach, Fla.)* **26**, 3433–3440 (2014).
- Lee, H. P. et al. Light-triggered in situ gelation of hydrogels using 2D Molybdenum Disulfide (MoS<sub>2</sub>) nanoassemblies as crosslink epicenter. *Adv. Mater.* **33**, 2101238 (2021).
- Jaiswal, M. K. et al. Vacancy-driven gelation using defect-rich nanoassemblies of 2D transition metal dichalcogenides and polymeric binder for biomedical applications. *Adv. Mater.* **29**, 1702037 (2017).
- Jaiswal, M. K., Singh, K. A., Lokhande, G. & Gaharwar, A. K. Superhydrophobic states of 2D nanomaterials controlled by atomic defects can modulate cell adhesion. *Chem. Commun.* **55**, 8772–8775 (2019).
- Brokesh, A. M. & Gaharwar, A. K. Inorganic biomaterials for regenerative medicine. *ACS Appl. Mater. Interfaces* **12**, 5319–5344 (2020).
- Carrow, J. K. et al. Photothermal modulation of human stem cells using light-responsive 2D nanomaterials. *Proc. Natl Acad. Sci.* **117**, 13329–13338 (2020).
- Ashburner, M. et al. Gene ontology: tool for the unification of biology. *Nat. Genet.* **25**, 25–29 (2000).
- Aleksander, S. A. et al. The gene ontology knowledgebase in 2023. *Genetics* **224**, iyad031 (2023).
- Rath, S. et al. MitoCarta3.0: an updated mitochondrial proteome now with sub-organelle localization and pathway annotations. *Nucleic acids Res.* **49**, D1541–D1547 (2021).
- Subramanian, A. et al. Gene set enrichment analysis: a knowledge-based approach for interpreting genome-wide expression profiles. *Proc. Natl Acad. Sci.* **102**, 15545–15550 (2005).
- Rohani, A., Kashatus, J. A., Sessions, D. T., Sharmin, S. & Kashatus, D. F. Mito Hacker: a set of tools to enable high-throughput analysis of mitochondrial network morphology. *Sci. Rep.* **10**, 18941 (2020).
- Wu, Z. et al. Mechanisms controlling mitochondrial biogenesis and respiration through the thermogenic coactivator PGC-1. *Cell* **98**, 115–124 (1999).
- Campbell, C. T., Kolesar, J. E. & Kaufman, B. A. Mitochondrial transcription factor A regulates mitochondrial transcription initiation, DNA packaging, and genome copy number. *Biochimica et.*

- Biophysica Acta (BBA)-Gene Regulatory Mechanisms* **1819**, 921–929 (2012).
35. Farr, C. L., Wang, Y. & Kaguni, L. S. Functional interactions of mitochondrial DNA polymerase and single-stranded DNA-binding protein: template-primer DNA binding and initiation and elongation of DNA strand synthesis. *J. Biol. Chem.* **274**, 14779–14785 (1999).
  36. Salvati, L. et al. Mitochondrial DNA depletion and dGK gene mutations. *Ann. Neurol.* **52**, 311–317 (2002).
  37. Antonenkov, V. D. et al. The human mitochondrial DNA depletion syndrome gene MPV17 encodes a non-selective channel that modulates membrane potential. *J. Biol. Chem.* **290**, 13840–13861 (2015).
  38. Jäger, S., Handschin, C., St.-Pierre, J. & Spiegelman, B. M. AMP-activated protein kinase (AMPK) action in skeletal muscle via direct phosphorylation of PGC-1 $\alpha$ . *Proc. Natl Acad. Sci.* **104**, 12017–12022 (2007).
  39. Salminen, A., Kaarniranta, K. & Kauppinen, A. Crosstalk between oxidative stress and SIRT1: impact on the aging process. *Int. J. Mol. Sci.* **14**, 3834–3859 (2013).
  40. Cai, W. et al. Oral advanced glycation endproducts (AGEs) promote insulin resistance and diabetes by depleting the antioxidant defenses AGE receptor-1 and sirtuin 1. *Proc. Natl Acad. Sci.* **109**, 15888–15893 (2012).
  41. Rodgers, J. T. et al. Nutrient control of glucose homeostasis through a complex of PGC-1 $\alpha$  and SIRT1. *Nature* **434**, 113–118 (2005).
  42. Li, Y. G. et al. Resveratrol protects cardiomyocytes from oxidative stress through SIRT1 and mitochondrial biogenesis signaling pathways. *Biochemical Biophysical Res. Commun.* **438**, 270–276 (2013).
  43. Almannai, M., El-Hattab, A. W., Ali, M., Soler-Alfonso, C. & Scaglia, F. Clinical trials in mitochondrial disorders, an update. *Mol. Genet. Metab.* **131**, 1–13 (2020).
  44. Wang, T. et al. Biosensor based on ultrasmall MoS<sub>2</sub> nanoparticles for electrochemical detection of H<sub>2</sub>O<sub>2</sub> released by cells at the nanomolar level. *Anal. Chem.* **85**, 10289–10295 (2013).
  45. Keeney, J. N., Winters, A. A., Sitcheran, R. & West, A. P. NF- $\kappa$ B-inducing kinase governs the mitochondrial respiratory capacity, differentiation, and inflammatory status of innate immune cells. *J. Immunol.* **210**, 1123–1133 (2023).
  46. Cohen-Gould, L. A stable lead citrate stain for grids. *Microsc. Today* **13**, 46–47 (2018).
  47. Dobin, A. et al. STAR: ultrafast universal RNA-seq aligner. *Bioinformatics* **29**, 15–21 (2013).
  48. Gentleman, R. C. et al. Bioconductor: open software development for computational biology and bioinformatics. *Genome Biol.* **5**, 1–16 (2004).
  49. Anders, S. & Huber, W. Differential expression analysis for sequence count data. *Nature Precedings*, 1–1 (2010).
  50. Falcon, S. & Gentleman, R. Using GStats to test gene lists for GO term association. *Bioinformatics* **23**, 257–258 (2007).
  51. Zhou, Y. et al. Metascape provides a biologist-oriented resource for the analysis of systems-level datasets. *Nat. Commun.* **10**, 1523 (2019).
  52. Hahne, F. & Ivanek, R. Visualizing genomic data using Gviz and bioconductor. *Statistical genomics: methods and protocols*, **1418**, 335–351 (2016).
  53. Ahuja, M. et al. Distinct Nrf2 signaling mechanisms of fumaric acid esters and their role in neuroprotection against 1-methyl-4-phenyl-1, 2, 3, 6-tetrahydropyridine-induced experimental Parkinson's-like disease. *J. Neurosci.* **36**, 6332–6351 (2016).
  54. Gohil, V. M. et al. Nutrient-sensitized screening for drugs that shift energy metabolism from mitochondrial respiration to glycolysis. *Nat. Biotechnol.* **28**, 249–255 (2010).
  55. Gohil, V. M. et al. Mitochondrial and nuclear genomic responses to loss of LRPPRC expression. *J. Biol. Chem.* **285**, 13742–13747 (2010).

## Acknowledgements

All the figures were organized in Adobe Illustrator. Portions of this research were conducted with the advanced computing resources provided by Texas A&M High Performance Research Computing. We would also like to acknowledge the use of Texas A&M University Microscopy and Imaging Center Core Facility (RRID:SCR\_022128) for confocal and electron microscopy. A.K.G. acknowledges financial support from the National Institute of Biomedical Imaging and Bioengineering (DP2 EB026265), the National Institute of Dental and Craniofacial Research (R01 DE032031), Peer Reviewed Medical Research Program (PRMRP) of Department of Defense (DOD) (W81XWH2210932), President's Excellence Fund (X-Grants) from Texas A&M University. V.M.G. acknowledges financial support from the NIH (R01GM143630; R35GM152102), the Welch Foundation (A-1810) and the President's Excellence Fund (X-Grants) from Texas A&M University. I.S. acknowledge financial support from the National Institute of Neurological Disorders and Stroke (NINDS) (R21 NS121945), the National Cancer Institute (NCI) (R01 CA282251) and Cancer Prevention and Research Institute of Texas (CPRIT RP230204). H.C.K. acknowledges financial support from the National Science Foundation (NSF) (1648451) and the College of Engineering of Texas A&M University. The content is solely the responsibility of the authors and does not necessarily represent the official views of the funding agencies.

## Author contributions

A.K.G., V.M.G., and I.S. contributed to conceptualization, supervision, funding, investigation, visualization, and writing. K.A.S. led the conceptualization, experimental design, methodology, investigation, visualization, and writing. J.S., M.Z., G.L., S.G., A.M., N.M.G., H.K., J.N.K., and R.S. contributed to the methodology and investigation. R.B. led the cyclic voltmeter and amperometric analysis under the supervision of H.C.K. K.A.S., and A.L.K. led the computational analysis and data processing under the supervision of I.S. All coauthors commented on the results and critical revision of the manuscript.

## Competing interests

The authors declare the following competing interests. A.K.G., K.A.S., V.M.G., and I.S. have filed a patent application related to the work presented in this article. The remaining authors declare no competing interests.

## Additional information

**Supplementary information** The online version contains supplementary material available at <https://doi.org/10.1038/s41467-024-52276-8>.

**Correspondence** and requests for materials should be addressed to Irtisha Singh, Vishal M. Gohil or Akhilesh K. Gaharwar.

**Peer review information** *Nature Communications* thanks Jiajie Diao, Meike Mevissen and the other, anonymous, reviewer(s) for their contribution to the peer review of this work. A peer review file is available.

**Reprints and permissions information** is available at <http://www.nature.com/reprints>

**Publisher's note** Springer Nature remains neutral with regard to jurisdictional claims in published maps and institutional affiliations.

**Open Access** This article is licensed under a Creative Commons Attribution-NonCommercial-NoDerivatives 4.0 International License, which permits any non-commercial use, sharing, distribution and reproduction in any medium or format, as long as you give appropriate credit to the original author(s) and the source, provide a link to the Creative Commons licence, and indicate if you modified the licensed material. You do not have permission under this licence to share adapted material derived from this article or parts of it. The images or other third party material in this article are included in the article's Creative Commons licence, unless indicated otherwise in a credit line to the material. If material is not included in the article's Creative Commons licence and your intended use is not permitted by statutory regulation or exceeds the permitted use, you will need to obtain permission directly from the copyright holder. To view a copy of this licence, visit <http://creativecommons.org/licenses/by-nc-nd/4.0/>.

© The Author(s) 2024